Substitutional nitrogen atom in diamond. A quantum mechanical investigation of the electronic and spectroscopic properties

Substitutional Nitrogen Atom in Diamond. A Quantum Mechanical Investigation of the Electronic and Spectroscopic Properties

Anna Maria Ferrari,[1,*] Simone Salustro,[1] Francesco Silvio Gentile,[1] William C. Mackrodt,[1] and Roberto Dovesi[1]

[1] *Dipartimento di Chimica, Università di Torino and NIS (Nanostructured Interfaces and Surfaces) Centre, Via P. Giuria 5, 10125 Torino, Italy*

(Dated: March 29, 2018)

This paper reports the fully-relaxed lattice and electronic structures, vibrational spectra, and hyperfine coupling constants of the substitutional N_s defect in diamond, derived from B3LYP calculations constructed from *all-electron* Gaussian basis sets and based on periodic supercells. Mulliken analyses of the charge and spin distributions indicate that the defect comprises a single unpaired electron distributed very largely over both the negatively-charged substituted site and one of the four nearest-neighbour carbon sites, which relaxes away from the impurity. This leads to a local C_{3v} symmetry, with the nitrogen 'lone pair' lying along the C_3 axis and pointed towards the 'dangling' bond of the shifted carbon neighbour. The calculated band gap is 5.85 eV, within which a singly-occupied, majority spin donor band is found ∼2.9 eV above the valence band, and an unoccupied, minority spin acceptor band ∼0.9 eV below the conduction band. Atom-projected densities of states of the donor and acceptor levels show that, contrary to a widespread description, ∼30% only of the donor band derives from nitrogen states *per se*, with the majority weight corresponding to states associated with the shifted carbon atom. The defect formation energy is estimated to be ∼3.6 eV. The calculated IR spectrum of the impurity centre shows several features between 800 and 1400 cm^{-1}, all of which are absent in the perfect crystal, for symmetry reasons. These show substantial agreement with recent experimental observations. The calculated hyperfine constants related to the coupling of the unpaired electron spin to the N and C nuclei, for which the Fermi contact terms vary from over 200 MHz to less than 3 MHz, are generally in good agreement with the largest experimental values, both in terms of absolute magnitudes and site assignments. The agreement is less good for the smallest two values, for which the experimental assignments are less certain. The results lend support to previous suggestions that some of the weaker lines in the observed spectra, notably those below ∼7 MHz, which are difficult to assign unambiguously, might result from the overlap of lines from different sites.

1. INTRODUCTION

Diamond, with its high melting point, chemical stability, wide band gap, high carrier mobility and optical transparency in the Infrared (IR), is an attractive candidate for application in numerous areas of technological importance, including high temperature diodes, microwave transistors, thermistors and radiation detectors.[1,2] Consequently, these extreme properties, which can often be related to the presence of intrinsic and extrinsic defects and can be incorporated in both natural and synthetic diamond despite the strength of the C-C bonding,[3–8] have been the subject of widespread and sustained theoretical and experimental interest.[5–18] Of the many and varied experimental techniques that are available, IR and Raman spectroscopy have been shown to be particularly suited to the attempted characterisation of the atomic nature of point-defects in diamond-like materials.[6,7,12,16,17,19–25]

Nitrogen is the most common impurity in diamond, leading to numerous phases which are characterised by the content and atomic nature of the impurity. In type *Ib* diamond, isolated nitrogen atoms substitute single carbon atoms[26,27], giving the substitutional defect, N_S, also referred to as C centres; they are the simplest nitrogenous defect in diamond. However, pure natural *Ib* diamonds are extremely rare, for high geological temperatures and pressures promote aggregation, first to vicinal N_S pairs, known as A aggregates, which, at more extreme conditions, coalesce to form so-called B aggregates, in which four N_S surround a carbon vacancy. In addition, during B aggregation, a side reaction also leads to the formation of N_3 aggregates, in which three N_S impurities are bound to a carbon vacancy.[28,29] On the other hand, synthetic diamonds produced by CVD (carbon vapour deposition) and controlled HTHP (high temperature high pressure) grow generally as type *Ib*, but often, with minor amounts of other defects.[30]

The single substitutional defect, N_S, leads to a distinctive IR spectrum with characteristic vibrational modes[31–38] at 1130 and 1344 cm^{-1}; it also gives rise to the P1 electron paramagnetic resonance (EPR) signal, which is how it was first discovered in 1959.[39] Both the early EPR and subsequent ENDOR studies[39–43] have shown that the P1 centre has an effective spin of $S = \frac{1}{2}$, a C_{3v} symmetry with the nitrogen atom, N_S, displaced away from one of its four neighbours, and that most of the unpaired spin is located on just one of the carbon atoms neighbouring N_S. Correlations between the intensity of the 1130 cm^{-1} peak and the N_S content derived from EPR experiments have established that P1 and C centres are unambiguously the same defect.[44,45]

The structure of the N_S defect has been confirmed by several *ab initio* calculations[47–50], which show that it consists of a single nitrogen atom bonded to three carbon

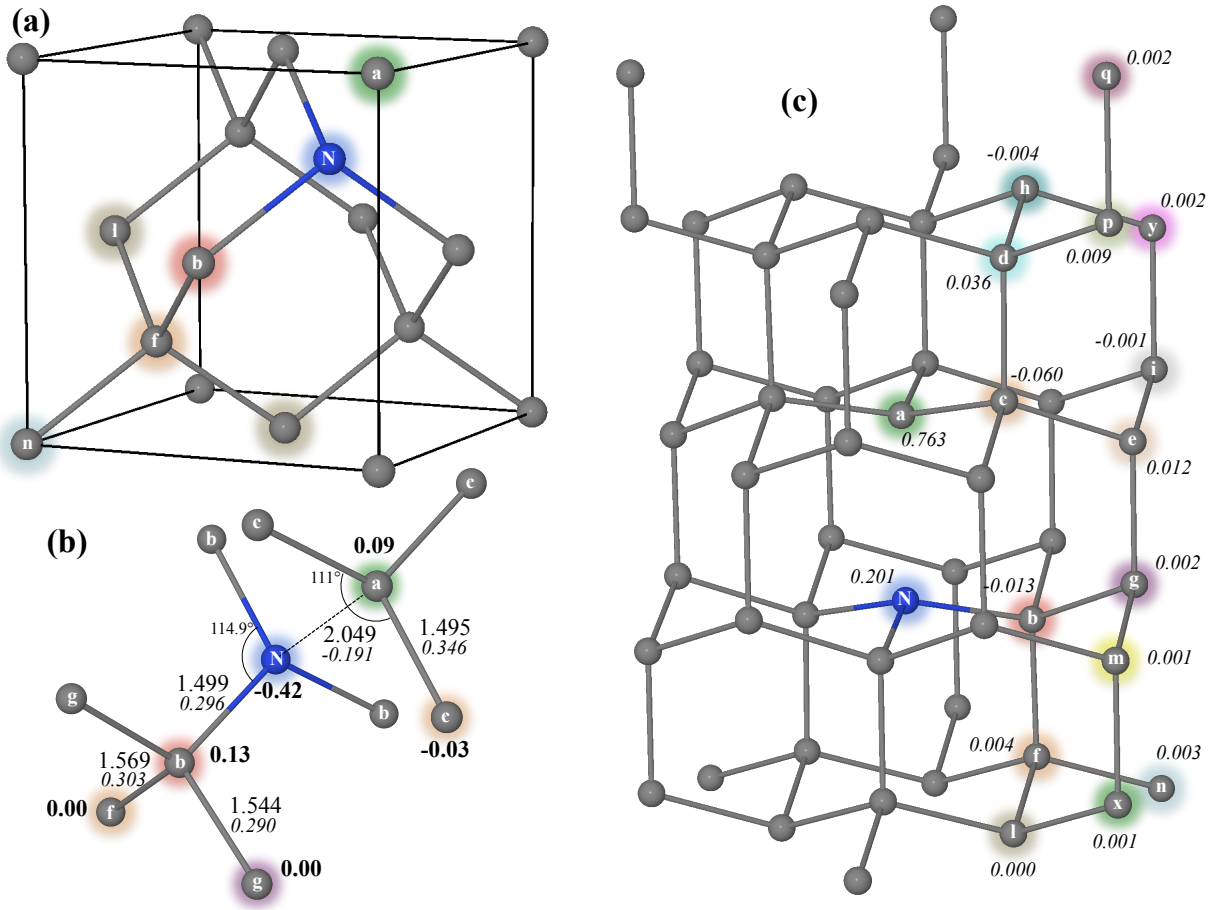

FIG. 1: The C-centre in the pristine diamond conventional cell (a) and the local cluster around the defect ((b) and (c); (c) shows a larger atomic cluster surrounding the defect, with the labelling of atoms reported in Refs. 39–42 and 46. The local point symmetry at N is C_{3v}. Mulliken net charges (b) and spin momenta (c) (in $|e|$, **bold** and *italic* respectively) are reported for each symmetry irreducible atom. Bond distances and Mulliken bond populations (in Å and $|e|$, *italic*, respectively) are reported in (b) below each pair of atoms.

neighbours. The nitrogen lone-pair orbital and that of the un-coupled 'dangling' bond electron of the furthermost carbon neighbour are directed towards each other forming a fourth, more extended N-C *bond*, which is calculated to be between 24% and 32% longer than the C-C bond in diamond. It is this chemical re-construction that is believed to drive the energy of the donor, namely the un-coupled electron, deep into the band gap, some 1.7 eV - 2.2 eV below the conduction band minimum according to photoconductivity[51] and optical spectra measurements.[52]

However, it is important to recognise that neither of these sets of measurements can reveal the detailed electronic structure of the donor level. Clearly it is the result of nitrogen insertion into the diamond lattice, but may not be a nitrogen level *per se*. All previous calculations, whether finite cluster or periodic supercell, have been based on the simplest implementations of DFT, either LDA or PBE. However, these are known to describe poorly the exchange interaction, leading to appreciable underestimates of the band gap, which is precisely where the defect states are located.

Conversely, recent quantum-mechanical characterization of several point-defects in diamond[53–62] has shown a notable accuracy of hybrid functionals (which include in their formulation a certain percentage of *exact* exchange interaction) in predicting the electronic properties of these systems. Accordingly, the present paper reports new calculations of the charge and spin densities, band structure, IR and Raman frequencies and hyperfine coupling constant of the C centre (N_S) in diamond based on the energy-minimised atomic configuration of the defective lattice. The methodology comprises a combination of *all-electron* B3LYP electronic structure calculations for defective supercells containing up to 512 diamond units, and fully-analytic quantum mechanical methods for the *ab initio* evaluation of the IR and Raman spectra of solids.

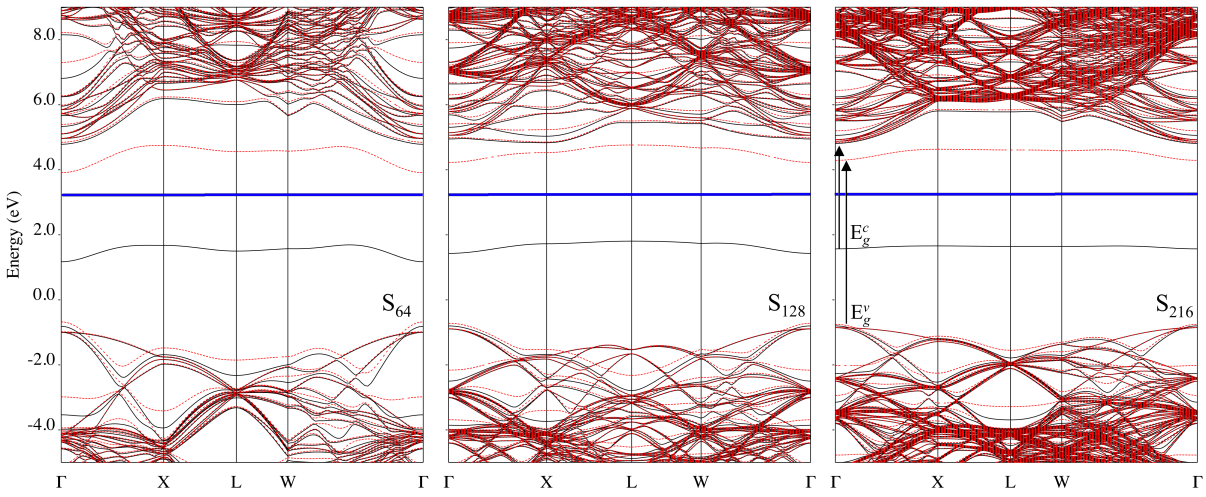

FIG. 2: B3LYP band structures of the C-centre in diamond for three different defect concentrations (S_{64}, S_{128} and S_{216}). The horizontal blue line marks the Fermi energy. Continuous (black) and dashed (red) lines correspond to spin-up and spin-down bands, respectively.

2. COMPUTATIONAL METHODS

For the most part, the DFT[63,64] calculations reported in this paper were based on the B3LYP global hybrid functional,[65,66] as implemented in the CRYSTAL program.[67] However, for comparison, selected features of the electronic properties of the N_s defect have also been examined using other DFT formulations based on pure LDA[68,69] and PBE[70], and the global PBE0[71] and range-separated HSE06[72] functionals. Pople's standard 6-21G[73] *all-electron* basis sets of Gaussian type functions have been adopted for both carbon and nitrogen, except for values of 0.23 and 0.30 Bohr^{-2} for the exponents of the outermost *sp* orbitals of the host and dopant atoms respectively. Again, for comparison and confirmation, two groups of additional basis sets have been examined. The first comprising, 6-21G, 6-31G and 6-31G*, was used to verify the N_s formation energy. The second, consisting of 6-31G-J* and 6-311G-J* bases[74], was employed for calculations of the electron-nuclear spin hyperfine coupling tensor (see below). These latter sets were designed with the explicit aim of creating small, but sufficiently accurate, basis sets for calculating spin coupling constants. They were derived from standard 6-31G and 6-311G bases by expanding the core functions followed by a new contraction of the valence functions.[74]

The truncation criteria of the Coulomb and exchange infinite lattice series are controlled by five thresholds, T_i, which have been set to 8 (T_1-T_4) and 16 (T_5). The convergence threshold on energy for the self-consistent-field (SCF) procedure has been set to 10^{-8} hartree for structural optimizations, while the convergence threshold has been set to 10^{-10} hartree for frequency calculations.

The DFT exchange-correlation contribution and its gradient are evaluated by numerical integration over the unit cell volume. The generation of the integration grid points is based on an atomic partition method, originally proposed by Becke[75], in which the radial and angular points are obtained from Gauss-Legendre quadrature and Lebedev two-dimensional distributions respectively. The choice of a suitable grid is crucial both for numerical accuracy and cost consideration. In this study a pruned grid with 75 radial and 974 angular points has been used.

The long-established supercell approach is used to simulate different defect concentrations. Here cells containing 64, 128, 216 and 512 atoms have been considered, and indicated as S_{64}, S_{128}, S_{216} and S_{512} in the following. Reciprocal space sampling is based on a regular Pack-Monkhorst[76] sub-lattice grid centred at the Γ point (*i.e.* at the center of the first Brillouin zone), leading to 4 (S_{64} and S_{128}) and 2 (S_{216} and S_{512}) sample points along each of the reciprocal lattice vectors, which corresponds to 13 and 4 **k**-points in the irreducible part of the Brillouin zone respectively, after point symmetry has been taken into account.

Harmonic phonon frequencies, ω_p at the Γ point are obtained from the diagonalization of the mass-weighted Hessian matrix of the second energy derivatives with respect to atomic displacements u:[77–81]

$$W^{\Gamma}_{ai,bj} = \frac{H^{\mathbf{0}}_{ai,bj}}{\sqrt{M_a M_b}} \quad \text{with} \quad H^{\mathbf{0}}_{ai,bj} = \left(\frac{\partial^2 E}{\partial u^{\mathbf{0}}_{ai} \partial u^{\mathbf{0}}_{bj}} \right) , \quad (1)$$

where atoms a and b (with atomic masses M_a and M_b) in the reference cell, **0**, are displaced along the i-th and j-th Cartesian directions, respectively. Integrated intensities for IR absorption $\mathcal{I}_p$ are computed for each mode p from the mass-weighted effective-mode Born-charge vec-

tor $\vec{Z}_p$[82,83] by means of the CPHF/KS relationship:[84,85]

$$\mathcal{I}_p \propto \left|\vec{Z}_p\right|^2 . \quad (2)$$

The relative Raman intensities of the peaks are computed analytically via a similar scheme.[86,87]
The coupling between the spin of the unpaired electron(s) (**S**) and the system of the nuclear spins (**I**) is described through the spin Hamiltonian:

$$H = \sum_n \mathbf{S} \cdot \mathcal{A}^n \cdot \mathbf{I}^n \quad (3)$$

where $\mathbf{I}^n$ and $\mathcal{A}^n$ refer to the nuclear spin and hyperfine coupling tensor related to the n^{th} nucleus, at site $\mathbf{R}_n$. $\mathcal{A}^n$ can be written in the form,

$$\mathcal{A}^n = A^n_{iso} \cdot \mathbb{1} + \mathcal{B}^n \quad (4)$$

where $\mathbb{1}$ is a 3×3 identity matrix, or

$$A^n_{ij} = A^n_{iso}\delta_{ij} + B^n_{ij} \quad (5)$$

where A^n_{iso} is the isotropic contribution to $\mathcal{A}^n$, often referred to as the *Fermi contact term*, and $\mathcal{B}^n$ the anisotropic dipole-dipole interaction of the electron and nuclear spins. The Fermi contact term for an unpaired electron

$$A^n_{iso} = \frac{8\pi}{3} g_e \mu_e g_n \mu_N |\psi(\mathbf{R}_n)|^2 \quad (6)$$

relates to the direct interaction of nuclear and electron spins, and is only non-zero for states with finite electron spin density, $|\psi(\mathbf{R}_n)|^2$, at nuclear sites $\mathbf{R}_n$, namely those with unpaired electrons in *s*-subshells. g_e, μ_e, g_n and μ_N are the free-electron *g*-factor, Bohr magneton, gyromagnetic ratio of $\mathbf{I}^n$ and the nuclear magneton respectively. The elements of the traceless tensor $\mathcal{B}^n$ at nucleus $\mathbf{R}_n$ are defined by:

$$B^n_{ij} = g_e \mu_e g_n \mu_N \int \mathrm{d}\mathbf{r}_n |\psi(\mathbf{r}_n)|^2 \left(\frac{3\mathbf{r}_{ni}\mathbf{r}_{nj} - |\mathbf{r}_n|^2 \delta_{ij}}{|\mathbf{r}_n|^5} \right) \quad (7)$$

where $\mathbf{r}_n$ is the distance to $\mathbf{R}_n$. $\mathcal{B}^n$ is usually written in terms of its three (principal axes) eigenvalues, B^n_1, B^n_2, B^n_3 and is a measure of the unpaired electron populations of valence *p* and *d* orbitals centred on the magnetic nucleus, and of all orbitals centred on neighbouring atoms. Clearly $A^n_{iso} = \frac{A^n_1 + A^n_2 + A^n_3}{3}$, since $\mathcal{B}^n$ is traceless, and, for a nuclear site with axial symmetry, we have $A^n_{iso} = \frac{A^n_{\parallel} + 2A^n_{\perp}}{3}$ and $B^n_{\parallel} + 2B^n_{\perp} = 0$.
An important point to note, especially with regard to electronic structure calculations, is that A^n_{iso} and B^n_{ij} impose different requirements on the wavefunction; for, whereas A^n_{iso} is determined by the electron density at the nuclear positions, as indicated in Equation 6, B^n_{ij} samples the long-range properties of the wavefunction as a result of the r^{-5} scaling in the integrand in Equation 7. It is essential, therefore, for basis sets to be sufficiently flexible so that these differing dependencies can be satisfied.

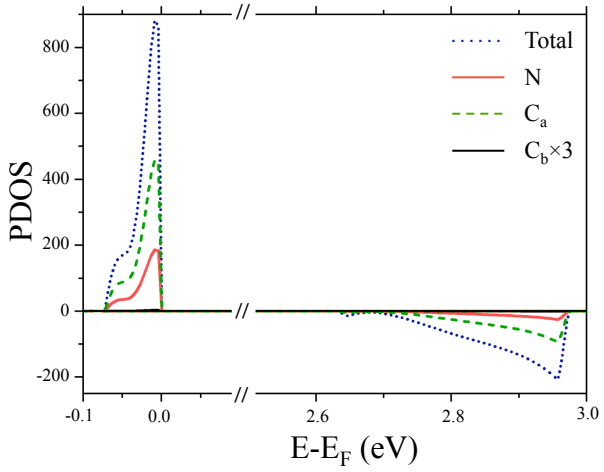

FIG. 3: Projected DOSs of the impurity states in the band gap computed with S_{216}. The C_b contribution is very low, and is superimposed to the zero line

3. RESULTS

3.1. Geometry, charge and spin densities, and band structure

The B3LYP geometry and electronic charge distribution of the optimised, neutral S_{216} supercell, and results from a Mulliken analysis, are shown in Figure 1. The substitution of a single carbon by nitrogen reduces the symmetry at the site from tetrahedral, T_d, (24 operations) to trigonal, C_{3v}, (6 symmetry operations), resulting in covalent bonds to three of the four nearest-neighbour (*nn*) carbon atoms (C_b in Figure 1). The nitrogen lone-pair, which points along the C_{3v} axis, prevents the formation of a covalent bond to the fourth adjacent carbon atom ($C_{(a)}$ in Figure 1), which now possesses a singly-occupied 'dangling' bond in the direction of the nitrogen. There is a concomitant change in the local geometry in which the three N-$C_{(b)}$ bond lengths and the three $C_{(a)}$-$C_{(c)}$ bond lengths, where $C_{(c)}$ is *nn* to $C_{(a)}$ (see Figure 1), are reduced from 1.560 Å to 1.499 and 1.495 Å, respectively. There is also a small reduction in the $C_{(b)}$-N-$C_{(a)}$ angle from the tetrahedral value of 109.47° to about 106.05°. On the other hand, the strong repulsion between the nitrogen lone pair and the unpaired electron of the 'dangling' bond leads to a substantial increase in the N-$C_{(a)}$ bond distance from 1.560 to 2.049 Å.
However, this local perturbation of the lattice decays rapidly, so that the bond distances of the $C_{(a)}$ second shells, namely, $C_{(c)}$-$C_{(d)}$ and $C_{(c)}$-$C_{(e)}$ are 1.556 Å, and of N, $C_{(b)}$-$C_{(f)}$=1.569 Å, respectively, values which are negligibly larger than in perfect diamond (1.560 Å). The net charges resulting from a Mulliken population analysis, also shown in Figure 1b, are -0.42 |*e*| on N, +0.13 |*e*| on $C_{(b)}$, while the second neighbour carbons are es-

sentially neutral. Similarly, the Mulliken populations on $C_{(a)}$ and $C_{(c)}$ (*nn* to $C_{(a)}$) are +0.09 $|e|$ and +0.03 $|e|$ and zero for farther neighbours. The N-$C_{(b)}$ bond population is +0.296 $|e|$, which is close to the corresponding C-C value in perfect diamond (+0.305 $|e|$) while the shorter N-C distance with respect to C-C compensates exactly the less covalent character of the bond as a result of its partial ionic nature. By comparison, the N-$C_{(a)}$ bond population, -0.191 $|e|$, indicates that the unpaired electron is located in an antibonding orbital. The spin density is localised largely on the carbon atom at the defect site ($C_{(a)}$, +0.763) and propagates along bonds in a smoothly damped way with non negligible values up to several shells of neighbours. Thus, from N outwards, the values of spin density are 0.201, -0.013, 0.004 and 0.002 $|e|$ on N, $C_{(b)}$, $C_{(f)}$, and $C_{(g)}$; and from $C_{(a)}$ outwards, +0.763, -0.060, 0.036, 0.012 and -0.004 $|e|$ on $C_{(a)}$, $C_{(c)}$, $C_{(d)}$, $C_{(e)}$ and $C_{(h)}$, as indicated in Figure 1c.

Figure 2 shows the band structures of the C-center for different sizes of supercell. The unpaired electron is localized in a very deep donor level approximately in the middle of the band gap, here calculated to be 5.85 eV, compared with the measured value of 5.4–5.6 eV,[31,52], resulting in an indirect band gap, E_g^c, of about 3.0 eV, which corresponds to the promotion of the electron in the defect level to the conduction band (see the arrow in Figure 2, right). There is also an associated acceptor level along the minority spin channel about 5 eV above the top of the valence band (direct gap E_g^v) that corresponds to the excitation of a hole from the empty impurity level to the top of the valence band, or equivalently, the promotion of an electron from the valence band to the empty defect level. The values of E_g^c and E_g^v are only marginally affected by the computational conditions (different hybrid Hamiltonians and basis set) and by the size of the supercell; however, the PBE and LDA (both pure DFT) gaps are considerably smaller, by about 2 eV, as might have been expected, see Table I.

What is perhaps the most interesting, and hitherto unreported, feature of the band structure of the C-center is shown in Figure 3, which contains the atom-projected densities of states of the donor and acceptor levels. This reveals that ∼30% only of the donor band and ∼20% of the minority spin acceptor band derive from nitrogen states *per se*. In both cases the majority contributions are from states associated with the nearest-neighbour carbon atom, $C_{(a)}$, which possesses a 'dangling' unpaired sp^3 orbital pointed towards N_s along the C_{3v} axis of the defect. While these $C_{(a)}$ states are clearly the *result* of nitrogen substitution, and as such, are part of the composite C-centre, they are not the iconic 'impurity' states as commonly interpreted, and designated in the general literature.

The ionization energy of the C-defect has been computed according to the Empirical Marker Method (EMM) and First Principles Marker Method (FPMM)[88] which compare the ionization potential of a defect with that of a known reference state. In the former approach the reference is the experimental ionization potential (IP) of another defect, which in the case of a shallow defect such as N_s, is usually taken as the phosphorus donor in diamond, for which the donor level has been reported as -0.6 eV below the conduction band, giving an IP of E_c-0.6 eV.[89] In the latter approach, the reference is a bulk diamond cell of the same size as that used to compute the defect energy, for which the donor level is the top of the valence band, E_c-E_g, and the acceptor level, the bottom of the conduction band, E_c or E_v+E_g. Based on a S_{512} supercell, the B3LYP hybrid and 6-21G basis sets, the computed EMM an FPMM ionisation potentials of N_s are E_c-2.0 eV and E_c-1.69 eV respectively, which are respectably close to the experimental value of E_c-1.7 eV reported by Farrer from photoconduction and optical absorption measurements[51] and to previous computed values.[88,90] The donor level of N_s is sufficiently high, $> 10^6$ K, to prevent spontaneous ionisation, which can only occur as a result of an external perturbation, such an electromagnetic field, or the presence of another defect with suitable energy levels that can act as an electron trap. The computed FPMM electron affinity of the acceptor level associated with N_s is E_c-1.1 eV or E_v+4.7 eV, again, in good agreement with previous calculations.[88,90] The acceptor state has been confirmed experimentally by Bonn *et al.*[91]

The computed ionization potential and electron affinity of the N_s donor and acceptor levels compare well with the strong thresholds, at 2.3 eV and 4.5 eV, measured in typical photoconductivity spectra from HPHT diamond.[52,92,93] The photocurrent threshold at 2.3 eV has been ascribed to the excitation of electrons, which can be compared with the N_s ionisation observed in absorption at 2.2 eV.[52,92,93] Similarly, the 4.5 eV threshold has been assigned to the excitation of holes[93], which fits comfortably with the broad absorption at 4.6 eV[94] attributed to the transition of electrons from the valence band to the acceptor level of N_s.

The formation energy of a defect (E_f) is usually defined as

$$E_f = (E_P - n \cdot E_C^i) - (E_D - m \cdot E_N^i) \qquad (8)$$

where E_P and E_D are the total energies of the pristine and defective diamond supercells, while E_C^i and E_N^i are the energies of the single carbon and nitrogen atoms, respectively; n is the number of carbon atoms eliminated, and m the number of nitrogen atoms added in the unit cell (in the present case $n = 1$ and $m = 1$). The superscript $i = 1, 2$ indicates two different ways to calculate the atomic energies. For $i = 1$, E_N^i and E_C^i are half of the total energy of the N_2 molecule for nitrogen and the energy of a single carbon atom in the pristine diamond structure, whereas for $i = 2$ they are the energies of the isolated atoms.

Table I contains formation energies based on S_{64} supercells for various functionals, from PBE0 to LDA, and basis sets, from 6-21G to 6-31G*, together with B3LYP/6-21G energies for supercells ranging from S_{128} to S_{512}. It

TABLE I: Defective energy gaps (E_g^c and E_g^v, see Figure 2), and formation energies (E_f^1 and E_f^2) obtained from two different procedures (see Equation 8 and the text) for the C-center defect in diamond. $E_g^{\rm Pure}$ is the gap of pure diamond. BS and SC stand for basis set and supercell. All data in are eV.

Method	BS	SC	E_f^1	E_f^2	E_g^c	E_g^v	$E_g^{\rm Pure}$
	6-21	S_{64}	3.59	6.79	3.01	4.59	5.56
	6-21	S_{128}	3.62	6.81	3.02	4.95	5.73
B3LYP	6-21	S_{216}	3.63	6.82	3.15	5.04	5.73
	6-21	S_{512}	3.63	6.82	3.22	5.22	5.76
	6-21*	S_{64}	3.69	6.44	3.09	4.50	5.75
	6-31*	S_{64}	3.22	5.59	3.20	4.57	5.91
PBE0	6-21	S_{64}	3.44	7.23	3.19	4.86	5.80
HSE06	6-21	S_{64}	3.43	7.21	2.46	4.23	5.17
PBE	6-21	S_{64}	3.28	6.74	1.06	3.02	4.09
LDA	6-21	S_{64}	2.67	6.86	0.91	2.93	4.03

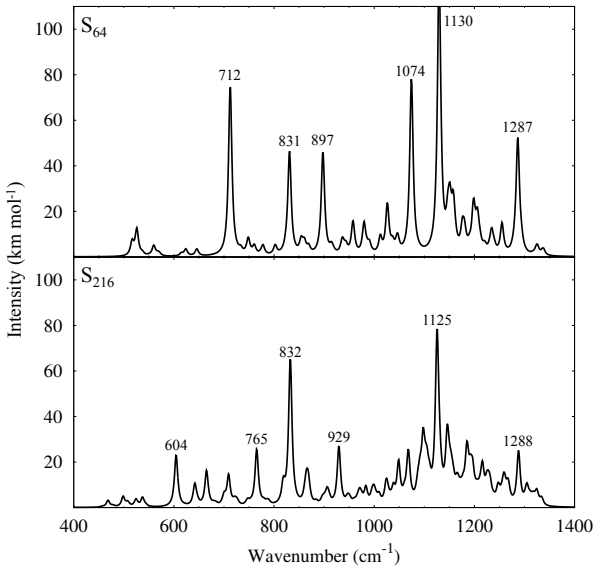

FIG. 4: Simulated IR spectra of the C-center in diamond for two different defect concentrations (S_{64} and S_{216}).

shows that, with the exception of LDA, all functionals provide formation energies that differ by less than 0.4 eV, that the formation energy is already well converged with the medium size supercell S_{64}, and that the use of larger basis sets such as 6-31G* can affect E_f^1 and E_f^2 by up to ∼0.4 and ∼1.2 eV, respectively.

Turning now to the formation energy of the C-centre, E_f^1, the B3LYP/6-21G value of 3.59 eV is comparable to energies of 3.72 eV and 3.66 eV computed for the A and B centres[57,58] using the same computational methods and conditions, although the latter defects are characterized by a larger N content (2 nitrogen atoms substituting two neighbouring carbon atoms in the A defect and 4 substitutional N facing a vacancy in the B defect). This proximity results from the high correlation energy of the N_2 molecule which is only partially taken into account by hybrid functionals. For the B-defect, containing 2 N_2 units, the 'correlation energy error' is twice that of the A defect. If the formation energy of the defect is evaluated directly from the isolated atom energies (E_f^2), the problem is bypassed, and the formation energies obtained for the C-defect are roughly one half those of the A-centre,[57] and one quarter those obtained for the B-centre,[58] *i.e.* 5.59 eV compared with 8.45 eV and 20.15 eV, respectively, at the B3LYP/6-31G* level (Table I).

3.2. Spectroscopic Characterization

1. IR and Raman spectra

As widely acknowledged, all real solids contain a large variety of defects ranging from dislocations and grain boundaries to point defects and impurities, at concentrations and homogeneities that are generally impossible to measure accurately; this is even more so for natural (as opposed to artificial) samples. One of the strengths of simulations is that both the type and concentration of defects are defined precisely *a priori* in any given study. This, of course, is one of the major differences between experimental and simulated spectra. With this as a background then, the first aim of this study was to examine the properties and features of the C-centre in diamond at various concentrations in the absence of (complicating) interactions with any other type of defect.

As a prelude to the analysis of our simulated spectra, it is useful to recall that the IR and Raman spectra of pristine diamond are particularly simple, for there are no permitted (or observed) IR transitions, as a result of the crystal symmetry, while the observed Raman spectra is characterised by a single intense peak at 1332[31] cm^{-1}, which compares favourably with a simulated value of 1317 cm^{-1} derived from B3LYP/6-21G calculations. Thus, any features that appear in the IR spectrum, and any additional features to the Raman spectrum are due to defects. This very simple perfect diamond reference, therefore, greatly facilitates the identification of the additional characteristics of individual defects in the simulated spectra of impure systems.

The simulated Raman spectrum of the C-centre (not shown) does not exhibit any sufficiently clear and distinctive additional features compared with pristine diamond, as is also the case of the A and B defects[57,58], for in all three cases the spectra are dominated by the 1317 cm^{-1} peak of the pure system. Consequently, the Raman spectrum is predicted to be of little value for the identification and characterisation of the N_s defect.

The IR harmonic vibrational spectra obtained at two defect concentrations corresponding to S_{64} and S_{216} are

shown in Figure 4. Looking at the S_{216} simulated spectrum, the 900-1400 cm^{-1} region is characterized by several peaks grouped around a central intense peak at around 1125 cm^{-1} and by a few less intense peaks in the 1300-1340 cm^{-1} region, that appear above the Raman frequency. The 900-400 cm^{-1} region is characterized by peaks with lower intensity with respect to those observed in the higher wavenumber region and only a signal at about 830 cm^{-1} seems to be significant in this spectral region. However, the fine structure of the S_{216} spectrum shows some, not negligible, differences by comparison with the spectrum for the smaller supercell, which suggests a verifiable dependence of the spectrum on the defect concentration.

Diamonds containing C-centres are rare in nature, though much more common in synthetic material, which, in the absence of a nitrogen 'getter', generally grows as type *Ib*, *i.e.* containing isolated N_s defects. In addition to the characteristic C-centre, such material also contains A-centres (vicinal N_s pairs), and, in some cases, X-centres, N^+).[30] Furthermore, additional components, D, E and F centers,[34] G, H and I centers[95], and recently a Y centre[36,37] have been further identified but not attributed to any specific defect. It is indeed clear that the identification of the unique features of a specific defect, such as the C-centre, in a pure IR spectrum is then not a simple task and requires a prior, or pre-existing, examination of a range of diamond samples by a decomposition procedure involving the subtraction of known spectral features of individual defect centres using one of the well assessed schemes proposed by Davies[96], Clark and Davey[34,95] and by Woods.[35]

The experimental spectrum of pure *Ib* diamond, taken from Ref. 97, is reported in Figure 5. The spectrum appears quite similar to those obtained through the deconvolution procedure by Clark and Davey[34] and Woods[35]. The main features of the infrared absorption are: (i) a sharp local-mode absorption peak close to 1344 cm^{-1}; (ii) a flattish hump between 1332 and 1200 cm^{-1}; (iii) a broad band peaking at 1130 cm^{-1} with a shoulder at 1092 cm^{-1}; (iv) a less intense signal at 1050 cm^{-1}; and (v) a broad weak hump centered at 832 cm^{-1}, see also Refs 34,38,98,99. To facilitate a comparison with experiment, a full simulated spectrum was obtained by enveloping each S_{216} frequency with a peudo-Voight function with a full width at half maximum of 30 cm^{-1}. A comparison of experimental[97] and simulated spectra is also shown in the same Figure 5, where a satisfactory match between the two is clearly evident, notably with regard to the distinctive features of the C-centre, which are correctly predicted, together with the low intense signals at 1050 and 832 cm^{-1}. The single point of disagreement concerns the absorption at 1344 cm^{-1}, which occurs as an intense spike in the experimental spectrum, but appears only as a few weak bands (even if well localized above the Raman frequency) in the simulations. This underlines the difficulty in extracting a pure C center spectrum since all spurious components could be not completely identified

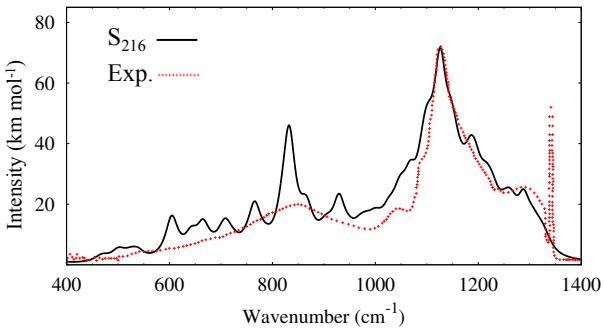

FIG. 5: Simulated IR spectra of the C-center in diamond for the S_{216} supercell with FWHM value of 30 cm^{-1}, compared with the experimental spectrum.[97]

and filtered out. In this regard, we note that the intensity of the 1344 cm^{-1} peak appears to be sample dependent; for instance, both Dyer[27] and Collins[32] report spectra with very low intensity at this frequency compared with the 1130 cm^{-1} band. In addition, while a linear correlation between the 1130 cm^{-1} band and the P1 EPR signals has been unambiguously established,[44,45] a similar correlation with the 1344 cm^{-1} has not been clearly reported in literature; thus, it not possible to exclude a correlation between the 1344 cm^{-1} peak and the content of dispersed N (in some way related to the C centre) but not specifically related to the P1 defect.
Finally, Collins and coworkers[32] reported a shift of 5 cm^{-1} to lower frequency for the peak at 1130 cm^{-1} (as expected from the ratio of the reduced masses), but no detectable shift for that at 1344 cm^{-1} in the spectra of ^{15}N doped samples. Again, calculations are able to shed light on this somewhat surprising behaviour. Figure 6 compares the simulated S_{216} spectra of normal (^{14}N) and ^{15}N isotopically substituted C-centres, where the shift of the 1130 cm^{-1} peak, by 2-4 cm^{-1}, and the unshifted 1344 cm^{-1} peak are clearly evident in the latter spectrum. This is supported by a normal coordinate analysis of the 1344 cm^{-1} vibration mode which indicates that the N atom remains stationary, and that only the surrounding C atoms move, probably/possibly as a result of a fortuitous balance of forces on N, as suggested previously by Collins.[33] Additionally, since the short $C_{(a)}$-$C_{(b)}$ bond is involved in the vibration, the normal mode is less strongly coupled to the lattice than the others, so that its frequency is pushed above the Raman frequency.

2. *The hyperfine coupling tensor*

There have been several reports of experimental values of A_{iso} and B_1, B_2 and B_3 for the hyperfine coupling of the spin density of the P1 centre (N_s) both to the central atoms, (^{14}N, ^{15}N) and $^{13}C_{(a)}$, and the surrounding C sites, derived from EPR and ENDOR measurements.[39–42,46] These are collected in Table II

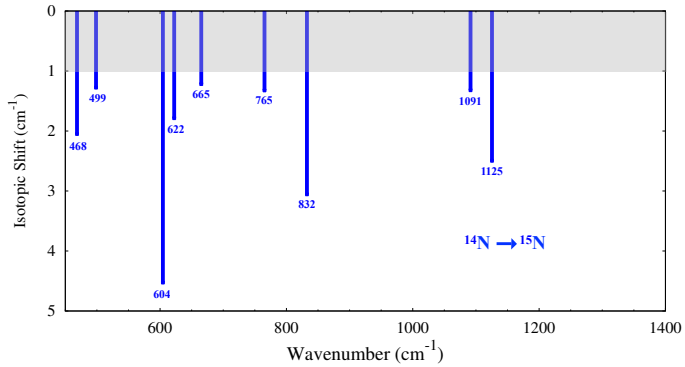

FIG. 6: Simulated isotopic shift due to ^{14}N→^{15}N substitution for the S_{216} supercell.

where the identities of the C sites, *a*, *b*, *c* etc. (given in brackets) correspond to those of Figure 1, while the subscripts, 1,2 .... 7, index the values of A_{iso} in descending order of magnitude. At first sight, the calculated unpaired electron spin density of the P1 centre is consonant with these results, for, as Figure 1 shows, a small, but non-negligible (4%) part of the spin density extends over the six sites nearest neighbour to the central atoms of the centre, with 20% at N and 76% at $C_{(a)}$. While there is no dispute as to the assignments at N and $C_{(a)}$, those at other C sites are less certain, so that, as discussed later in this section, the present calculations offer the possibility of alternative assignments for some of the peripheral sites. However, before considering the dependence of the components of the hyperfine tensor, $\mathcal{A}$, on the details of the calculated spin density distribution, it is useful, to examine how $\mathcal{A}$ depends on computational variables such as the hybrid functional, basis set, supercell size and geometry relaxation, to help choose a computational approach that balances affordability of calculation with accuracy of results. To the best of our knowledge, there are no reports in the diamond defects literature of such dependence, so that the variation in the computed values of A_{iso} and B_1, B_2 and B_3 given in Tables III, IV and V cannot be assessed against previous calculations, but solely on experimental data.[39–42,46] The significance of this latter observation is that the fortuitous cancellation of errors, notably for limited sample sets, is not uncommon in the defect literature, so that an independent computationally-based verification of the trends we find in this study would have been useful.

Calculated values of A_{iso}, B_1, B_2 and B_3 derived from basis sets, including 6-21G, 6-21G*, 6-31G*, 6-31G-J* and 6-311G-J*, and functionals, which include LDA, PBE, B3LYP, PBE0, HSE06 and F35LYP, are collected in Tables III and IV, where F35LYP corresponds to a modified B3LYP functional with 35% exact exchange compared with the 'standard' 20%. Both Tables are based on fully relaxed S_{64} supercells. To reduce the number of calculations to manageable proportions, the complete set of (basis set/functional) combinations was truncated, so that the basis set dependence was restricted solely to the B3LYP functional (Table III), and the functional dependence solely to the 6-311G-J* basis set (Table IV).

TABLE II: Experimental hyperfine coupling constants (MHz) for the P1 defective center. The labels in round brackets are those shown in Figure 1. $\mathcal{B}$ tensor components are sorted so that $|B_1| > |B_2| > |B_3|$.

Atom	A_{iso}	B_1	B_2	B_3	Ref.
^{14}N	92.6	21.6	-10.8	-10.8	[39]
	92.2	21.8	-10.9	-10.9	[46]
	92.2	21.8	-10.9	-10.9	[41]
^{15}N	-129.1	-30.6	15.3	15.3	[41]
$^{13}C_1$ (*a*)	208.2	132.1	-66.1	-66.1	[39]
	208.1	132.7	-66.3	-66.3	[42]
	205.7	132.4	-66.2	-66.2	[41]
$^{13}C_2$ (*d*)	35.5	7.0	-3.5	-3.5	[40]
	35.2	6.2	-3.1	-3.1	[42]
	34.3	6.0	-3.4	-3.0	[41]
$^{13}C_3$ (*c*)	25.8	-	-	-	[40]
	25.6	-2.3	1.2	1.2	[42]
	24.9	-2.1	1.6	0.5	[41]
$^{13}C_4$ (*b*)	13.5	-	-	-	[40]
	11.8	2.3	-1.2	-1.2	[41]
	12.3	2.2	-1.1	-1.1	[42]
$^{13}C_5$ (*g* or *e*)	8.2	–	–	–	[42]
	9.5	2.3	-1.4	-0.9	[41]
$^{13}C_6$ (*f*)	4.1	–	–	–	[42]
$^{13}C_7$ (*g* or *e*)	2.7	–	–	–	[42]

Starting with the basis set dependence, the comparison of Table II and Table III shows that there is a clear demarcation between the N and C_1-C_5 values of the hyperfine constants and those corresponding to C_6 and C_7. For the former, overall there is good agreement between the calculated and observed values of A_{iso}, B_1, B_2 and B_3, notably the dipole-dipole terms, with two caveats. The first is that the calculated C_3 Fermi contact terms are negative, whereas the reported values from ENDOR[41] and EPR[42] are both positive. However, Cox *et al.*[41] have pointed out that EPR and ENDOR cannot distinguish between differences in the sign of A_{iso} (at any site); moreover, they suggest that possible explanations for the

TABLE III: B3LYP computed hyperfine coupling constants (MHz) for the P1 defect centre derived from different basis sets. The values correspond to S_{64} supercells fully optimized at the computational level indicated in each entry of the table. $\mathcal{B}$ tensor components are sorted so that $|B_1| > |B_2| > |B_3|$. The labels in round brackets are those shown in Figure 1.

Site	Basis Set	A_{iso}	B_1	B_2	B_3
^{14}N	6-21G	93.95	19.28	-9.64	-9.64
	6-21G*	90.19	18.42	-9.21	-9.21
	6-31G*	71.86	20.69	-10.34	-10.34
	6-31G-J*	81.95	22.16	-11.08	-11.08
	6-311G-J*	81.46	23.47	-11.73	-11.73
^{13}C$_1$ (a)	6-21G	303.48	110.44	-55.22	-55.22
	6-21G*	268.06	112.28	-56.14	-56.14
	6-31G*	243.79	127.68	-63.84	-63.84
	6-31G-J*	208.87	137.88	-68.94	-68.94
	6-311G-J*	206.76	138.44	-69.22	-69.22
^{13}C$_2$ (d)	6-21G	40.58	5.25	-2.88	-2.37
	6-21G*	34.80	5.34	-2.92	-2.42
	6-31G*	30.93	5.93	-3.20	-2.73
	6-31G-J*	34.94	6.35	-3.40	-2.95
	6-311G-J*	34.45	6.20	-3.34	-2.86
^{13}C$_3$ (c)	6-21G	-32.66	2.56	-1.57	-0.99
	6-21G*	-28.67	2.72	-1.89	-0.83
	6-31G*	-24.14	2.33	-1.63	-0.70
	6-31G-J*	-24.37	2.10	-1.46	-0.63
	6-311G-J*	-24.53	2.44	-1.66	-0.78
^{13}C$_4$ (p)	6-21G	13.38	1.54	-0.90	-0.64
	6-21G*	12.59	1.71	-0.97	-0.74
	6-31G*	10.64	1.89	-1.07	-0.82
	6-31G-J*	10.25	1.99	-1.12	-0.87
	6-311G-J*	10.36	2.01	-1.13	-0.88
^{13}C$_5$ (e)	6-21G	12.02	2.11	-1.21	-0.90
	6-21G*	10.24	2.08	-1.21	-0.87
	6-31G*	9.17	2.24	-1.31	-0.93
	6-31G-J*	9.65	2.34	-1.36	-0.98
	6-311G-J*	9.66	2.32	-1.37	-0.95
^{13}C$_6$ (n)	6-21G	6.99	0.60	-0.39	-0.21
	6-21G*	6.30	0.65	-0.41	-0.25
	6-31G*	5.58	0.70	-0.41	-0.29
	6-31G-J*	5.16	0.73	-0.42	-0.31
	6-311G-J*	5.19	0.73	-0.40	-0.32
^{13}C$_7$ (f)	6-21G	4.46	1.02	-0.54	-0.48
	6-21G*	3.52	1.00	-0.51	-0.48
	6-31G*	3.66	1.02	-0.52	-0.51
	6-31G-J*	4.71	1.05	-0.53	-0.52
	6-311G-J*	4.63	1.02	-0.52	-0.50
^{13}C$_8$ (b)	6-21G	-5.18	1.83	-1.12	-0.72
	6-21G*	-5.10	1.84	-1.17	-0.67
	6-31G*	-4.21	1.80	-1.12	-0.68
	6-31G-J*	-4.21	1.75	-1.07	-0.68
	6-311G-J*	-4.11	1.76	-1.11	-0.65

different measured values of the components of A_{iso} at $C_{(b)}$ require these to be negative. The second is that both EPR[42] and ENDOR[41] measurements assign C_4 to site (b), whereas all the calculations reported here assign C_4 to site (p), even though this is further from the central sites, N and $C_{(a)}$. We postpone a discussion of this to later in the section where an overview of site assignment more generally is given. It is clear that the 6-21G basis set performs least satisfactorily across the entire range of N and C_1-C_5 coupling constants, with the largest errors occurring for A_{iso}, which is systematically overestimated. The Fermi contact terms require the greatest computational accuracy, but are, perhaps, the most significant of the coupling constants, for they are most readily compared with the observed values. The values at the C sites are larger than experiment by 20-30%, but by considerably less for the N site, 1-2%. As the 6-21G* and 6-31G* results show, the addition of a polarisation function to the basis sets reduces the errors of the calculated constants, but now, A_{iso} for all sites, other than C_1, are lower than the experimental values.[41]

The best performances are provided by 6-31G-J*: on all the C centers the computed Fermi contact terms are in comfortable agreement with the corresponding experimental values although the N values and C_4 values are respectively, significantly underestimated and overestimated by ∼10%. Calculations with the larger 6-311G-J* do not lead to any significant improvement with respect to 6-31G-J*.

For C_6 and C_7, which, from Table II, are the lowest two experimental values of A_{iso} and have been assigned to sites (f), and (g) or (e), respectively, we find the greatest discrepancies with our calculations. First, there are no values of the contact term down to the eighth lowest calculated, designated in Table III in the interests of simplicity as C_8, which approach the (experimental) $C_{7(g,e)}$ value of 2.7 MHz, so that this is unaccounted for within our reported results. For $C_{6(f)}$ (4.1 MHz) of Table II there are two contenders, $C_{8(b)}$ (-4.11 MHz), and $C_{7(f)}$ (4.63 MHz) in the list of calculated Fermi contact terms in Table III. Of these, the value of C_8 is chosen for the purposes of comparison with other functionals (see Table IV below). Concerning the dipole-dipole terms, all five basis sets give a good account of their values, with differences generally <10% between them.

Turning now to a comparison of different functionals, Table IV lists the calculated values of A_{iso}, B_1, B_2 and B_3 using the 6-31G-J* basis set, again, based on fully relaxed S_{64} supercell. Starting with sites N, C_1 - C_5, for which there are full sets of experimental data, four general points emerge. The first is that the four hybrid functionals are in good overall agreement with experiment. The second is that the B3LYP, PBE0 and HSE06 values are very similar, often, with differences between them that are comparable to the differences between the experimental values. The third is that increasing the proportion of exact exchange from 20% to 35% in the F35LYP functional increases the B3LYP estimates by ∼10%. The

fourth is that the pure DFT functionals, PBE and LDA, are the least satisfactory, the more so for LDA. The underestimates of the Fermi contact term, notably for $C_{(a)}$, underline the inability of functionals without significant degrees of exact exchange to localise spin density sufficiently at the nuclear sites. The sole exceptions are A_{iso} at the N site, which all the functionals underestimate by ∼10%. Concerning the experimental C_6 Fermi contact term, while all four hybrids lead to values (-4.25 MHz to -5.31 MHz) which approach experiment, 4.1 MHz, it is only F35LYP that predicts the correct order index (6).

The third computational variable we have sought to examine is supercell size, or, equivalently, defect concentration. Table V contains the four components of the hyperfine coupling tensor derived from fully optimised S_{64}, S_{216} and S_{512} supercells based on B3LYP/6-31G-J* calculations, including all C sites with $A_{iso} \geq 1.5$ MHz. The results therein indicate that the S_{216} and S_{512} constants are virtually indistinguishable and for N and C_1-C_5, which correspond to the innermost P1 sites, they are also very close to the S_{64} values. This suggests that for all intents and purposes, the values of these constants are independent of defect concentrations of less than one defect per sixty-four C atoms. However, from C_6 on, the S_{64} supercell starts to provide values of A_{iso} that can differ from the S_{216} and S_{512} ones, which are virtually identical.

While it is clearly important that calculations can account for the magnitudes of the P1 coupling constants, it is equally important that they affirm the site assignments, for, in some cases, these are less readily obtained from experiment with precision. Clearly, N and C_1 are unambiguously assigned, the latter to site (*a*), by virtue of the magnitude of the contact terms, which confirms that the unpaired electron is localised largely at these two sites of the P1 centre.

Tables II, III, IV, V collectively confirm the experimental assignment of C_2, C_3 and C_5 to sites (*d*), (*c*) rather than (*b*), and (*e*) respectively[41,42,46], with no differences between basis sets, functionals or supercell sizes. Of these, the C_2/C_3 assignments are somewhat surprising, for the unpaired *s*-electron density at nuclear site (d), which is within the 3^{rd} shell of neighbours from $C_{(a)}$, is 35.2 MHz[42], and that at nuclear site (c), which is within the 1^{st} shell of neighbours, 25.6 MHz[42]. Bower and Symons[43] have previously sought to explain this by a mechanism similar to hyperconjugation, in which the electron density at (d) is enhanced by the relatively large *p*-electron population at $C_{(a)}$. Bader spin population, reported in Table VI, can account reasonably for this effect as μ=-0.009 and 0.029 $|e|$ at sites $C_{(c)}$ and $C_{(d)}$, respectively.

Barklie *et al.*[42] and Cox *et al.*[41] assigned C_4 to either (*b*) or (*c*) from the multiplicity of the signal (3), and the positions of the 3 (*c*) and 3 (*d*) sites which are approximately axially symmetric about the [111] axis and not parallel to N-$C_{(a)}$. Since the present calculations have assigned C_3 to (*c*), the experimental assignments of C_4 can reasonably be taken as (*b*), whereas here, the predicted site

TABLE IV: 6-31G-J* computed hyperfine coupling constants (MHz) for the P1 defect centre derived from different Hamiltonians. The values correpond to S_{64} supercells fully optimized at the computational level indicated in each entry of the table. $\mathcal{B}$ tensor components are sorted so that $|B_1| > |B_2| > |B_3|$. The labels in round brackets are those shown in Figure 1. Note that the (b) site values correspond to different order positions of A_{iso} for the different functionals (6, 8, 13, 18)

Site		Method	A_{iso}	B_1	B_2	B_3
		B3LYP	81.95	22.16	-11.08	-11.08
		F35LYP	83.78	22.15	-11.08	-11.08
^{14}N		PBE0	86.00	21.75	-10.88	-10.88
		HSE06	85.94	21.75	-10.87	-10.87
		PBE	83.95	20.99	-10.50	-10.50
		LDA	82.56	21.85	-10.93	-10.93
		B3LYP	208.87	137.88	-68.94	-68.94
		F35LYP	228.32	143.76	-71.88	-71.88
$^{13}C_1$	(*a*)	PBE0	208.88	133.15	-66.58	-66.58
		HSE06	209.47	132.42	-66.21	-66.21
		PBE	175.68	120.56	-60.28	-60.28
		LDA	146.13	112.60	-56.30	-56.30
		B3LYP	34.94	-2.95	6.35	-3.40
		F35LYP	36.03	-3.08	6.52	-3.45
$^{13}C_2$	(*d*)	PBE0	34.25	-2.85	6.10	-3.26
		HSE06	34.12	-2.82	6.06	-3.25
		PBE	32.16	-2.47	5.55	-3.08
		LDA	30.18	-2.28	5.35	-3.07
		B3LYP	-24.37	2.10	-1.46	-0.63
		F35LYP	-28.60	1.92	-1.28	-0.64
$^{13}C_3$	(*c*)	PBE0	-25.88	1.85	-1.35	-0.50
		HSE06	-25.60	1.87	-1.37	-0.50
		PBE	-18.39	2.11	-1.67	-0.44
		LDA	-14.58	2.28	-1.95	-0.33
		B3LYP	10.25	1.99	-1.12	-0.87
		F35LYP	9.91	2.45	-1.40	-1.05
$^{13}C_4$	(*p*)	PBE0	10.88	2.02	-1.14	-0.88
		HSE06	10.99	2.01	-1.13	-0.88
		PBE	12.50	1.99	-1.06	-0.94
		LDA	12.15	1.87	-0.98	-0.89
		B3LYP	9.65	2.34	-1.36	-0.98
		F35LYP	9.77	1.99	-1.15	-0.84
$^{13}C_5$	(*e*)	PBE0	9.78	2.34	-1.38	-0.96
		HSE06	9.84	2.32	-1.37	-0.94
		PBE	9.41	2.12	-1.31	-0.81
		LDA	8.80	2.04	-1.26	-0.77
$^{13}C_8$		B3LYP	-4.21	1.75	-1.07	-0.68
$^{13}\mathbf{C_6}$		F35LYP	-5.31	1.74	-1.02	-0.73
$^{13}C_8$	(*b*)	PBE0	-4.37	1.83	-1.10	-0.73
$^{13}C_8$		HSE06	-4.25	1.83	-1.11	-0.73
$^{13}C_{13}$		PBE	-1.93	1.84	-1.21	-0.63
$^{13}C_{18}$		LDA	-0.46	1.87	-1.28	-0.59

TABLE V: The computed hyperfine coupling constants (MHz) for the P1 defect centre based on different supercells. The values correspond to supercells fully optimized at the B3LYP/6-31G-J* computational level. The labels in round brackets are those shown in Figure 1. Sites z and zz (not shown in Figure 1) are adjacent to sites m and i, respectively. Note that from C_6 on the decreasing order of A_{iso} for S_{64} can differ from the one of S_{216} and S_{216}. So for example A_{iso} for the (b) site (-4.21) is at C_8 for S_{64}, and at C_6 for S_{216} (-4.76) and for S_{512} (-4.73).

Atom	Label	Supercell	A_{iso}	B_1	B_2	B_3	Atom	Label	Supercell	A_{iso}	B_1	B_2	B_3
^{14}N		S_{64}	-114.96	-31.08	15.54	15.54	$^{13}C_7$	(f)	S_{64}	4.71	1.05	-0.53	-0.52
		S_{216}	-114.42	-30.93	15.47	15.47		(f)	S_{216}	4.10	1.09	-0.62	-0.46
		S_{512}	-114.14	-30.92	15.46	15.46		(f)	S_{512}	4.10	1.10	-0.65	-0.45
^{15}N		S_{64}	81.95	22.16	-11.08	-11.08	$^{13}C_8$	(b)	S_{64}	-4.21	1.75	-1.07	-0.68
		S_{216}	81.57	22.05	-11.02	-11.02		(n)	S_{216}	3.36	0.66	-0.36	-0.30
		S_{512}	81.37	22.04	-11.02	-11.02		(n)	S_{512}	3.35	0.69	-0.36	-0.33
$^{13}C_1$	(a)	S_{64}	208.87	137.88	-68.94	-68.94	$^{13}C_9$	(l)	S_{64}	2.92	0.32	-0.20	-0.12
	(a)	S_{216}	207.23	137.95	-68.98	-68.98		(i)	S_{216}	2.37	1.15	-0.66	-0.49
	(a)	S_{512}	206.58	138.06	-69.03	-69.03		(i)	S_{512}	2.38	1.14	-0.65	-0.49
$^{13}C_2$	(d)	S_{64}	34.94	6.35	-2.95	-3.40	$^{13}C_{10}$	(m)	S_{64}	2.47	0.33	-0.20	-0.13
	(d)	S_{216}	35.21	6.29	-3.46	-2.83		(h)	S_{216}	2.19	0.27	-0.18	-0.08
	(d)	S_{512}	35.24	6.28	-3.47	-2.81		(h)	S_{512}	2.24	1.47	-0.74	-0.73
$^{13}C_3$	(c)	S_{64}	-24.37	2.10	-1.46	-0.63	$^{13}C_{11}$	(i)	S_{64}	2.32	0.23	-0.17	-0.06
	(c)	S_{216}	-24.38	2.12	-1.50	-0.62		(m)	S_{216}	2.14	0.87	-0.52	-0.35
	(c)	S_{512}	-24.36	2.12	-1.50	-0.62		(m)	S_{512}	2.15	0.82	-0.49	-0.33
$^{13}C_4$	(p)	S_{64}	10.25	1.99	-1.12	-0.87	$^{13}C_{12}$	(z)	S_{64}	2.22	1.09	-0.62	-0.46
	(p)	S_{216}	10.46	2.16	-1.13	-1.04		(q)	S_{216}	1.97	0.64	-0.33	-0.31
	(p)	S_{512}	10.49	2.20	-1.12	-1.08		(q)	S_{512}	1.94	0.66	-0.36	-0.30
$^{13}C_5$	(e)	S_{64}	9.65	2.34	-1.36	-0.98	$^{13}C_{13}$	(zz)	S_{64}	1.40	-0.03	0.02	0.01
	(e)	S_{216}	9.56	2.37	-1.39	-0.98		(l)	S_{216}	1.88	0.70	-0.39	-0.31
	(e)	S_{512}	9.55	2.38	-1.40	-0.98		(l)	S_{512}	1.88	0.71	-0.38	-0.33
$^{13}C_6$	(n)	S_{64}	5.16	0.73	-0.42	-0.31	$^{13}C_{14}$	(g)	S_{64}	1.39	1.31	-0.70	-0.61
	(b)	S_{216}	-4.76	1.83	-1.19	-0.64		(g)	S_{216}	1.50	0.13	-0.10	-0.03
	(b)	S_{512}	-4.73	1.84	-1.21	-0.63		(g)	S_{512}	1.51	1.22	-0.63	-0.59

is (p). In support of the latter, we note that the (p) sites have the same orientation with respect to N-$C_{(a)}$ as the (b) sites, and, furthermore, that these are more closely linked to $C_{(a)}$ via 3 bonds, whereas (b) is linked via 4, Figure 1. Bader spin population supports this assignement since μ=-0.004 and 0.008 $|e|$ at sites $C_{(b)}$ and $C_{(p)}$, respectively, as shown in Table VI. In addition, Table V shows that the C_4 contact term derived from B3LYP/6-31G-J* calculations (10.25 MHz) matches comfortably the most accurate experimental value, 11.8 MHz, by Cox *et al.*[41]

Turning now to the C_6 and C_7 hyperfine coupling, there are experimental values only for the Fermi contact term, even though none of the interactions is purely isotropic. However, the complexity of the spectra in this frequency range has restricted the information that has been retrieved. Barklie *et al.*[42] have attributed the C_6 contact term to site (f), which coincides with that predicted here for C_7. However, we note that our calculated values (see Table V) of $C_{6(b)}$ and $C_{7(f)}$, -4.73 MHz and 4.10 MHz respectively, are sufficiently close to the reported experimental values of 4.1 MHz[42], so that we hypothesise that the corresponding EPR and ENDOR signals may be the results of overlapping signals from these two sites. Furthermore, Barklie *et al.*[42] have suggested that the intensity of the lines that contribute to C_7 result from the overlap of spectral intensity arising from several sites, a view which the present paper endorses.

Finally, with regard to the calculated hyperfine constants corresponding to C_8 to C_{14}, we note that Cox *et al.*[41]

TABLE VI: List of neighbours and their distances d (in Å) with respect to the defect sites a (C_a) and N. For each atom the site label corresponds to that in Figure 1 and the multiplicity given in round brackets. Mulliken and Bader spin densities μ (in $|e|$) are also reported.

Neighbour	-	1	2	3	4	5	6	7	8	9	10	11	...	-
Site	a	c (3)	N	d (3)	e (6)	h (3)	b (3)	i (3)	g (6)	y (3)	m (3)	p (3)	-	q (3)
d	0.	1.495	2.049	2.385	2.543	2.791	2.802	2.947	3.113	3.466	3.756	3.782	-	4.906
μ (Mulliken)	0.763	-0.060	0.201	0.036	0.012	-0.004	-0.013	-0.001	0.002	0.002	0.001	0.009	-	0.002
μ (Bader)	0.605	-0.009	0.206	0.029	0.009	0.000	-0.004	0.000	0.001	0.002	0.001	0.008	-	0.001
Site	N	b (3)	a	f (3)	g (6)	l (3)	m (3)	e (6)	x (3)	i (3)	n (3)			
d	0.	1.499	2.049	2.400	2.536	2.811	2.951	3.106	3.479	3.740	3.794			
μ (Mulliken)	0.201	-0.013	0.763	0.004	0.002	0.000	0.001	0.012	0.001	-0.001	0.003			
μ (Bader)	0.206	-0.004	0.605	0.003	0.001	0.001	0.001	0.009	0.000	0.000	0.002			

have reported that ENDOR measurements from 7.5 MHz to 1 MHz revealed transitions from many weakly coupled ^{13}C sites, but were not possible to interpret with certainty.

A similar assignment has been recently proposed by Goss and Briddon[50] based on a generalized-gradient-approximation density functional. However in that study the largest Fermi contact components did not always have an experimental counterpart so that the correspondence between computed and observed values were established largely by a 'best fit' procedure, thus losing the full predictive power of the calculations.

4. CONCLUSION

This work, based on all electron, Gaussian type orbitals, B3LYP calculations and periodic supercells has provided an accurate description of the lattice and band structures, charge and unpaired spin density distributions and vibrational frequencies of the nitrogen substitution defect, N_s, in diamond by comparison with available photoconduction and optical absorption[51,52,93], IR[27,32,33,36–38] and Raman[31], and EPR[42] and ENDOR[41,43] data.

In the C center, substitutional N forms covalent bonds to three of the four nearest neighbour carbons, which are shorter than in pristine diamond, while the nitrogen 'lone pair' prevents the formation of a covalent bond to fourth carbon, which bears the 'dangling' bond. The local symmetry is C_{3v}, with the nitrogen 'lone pair' lying along the C_3 axis and pointed towards the 'dangling' bond of the carbon neighbour along this axis, which is shifted away from the nitrogen by 0.49 Å.

N substitution leads to a deep singly-occupied, majority spin donor band at ∼2.9 eV above the valence band, and an unoccupied, minority spin acceptor band ∼0.9 eV below the conduction band, values not affected by the choice of hybrid Hamiltonians and basis sets. Atom-projected densities of states of the donor and acceptor levels show that, contrary to a widespread description of these states, ∼30% only of the donor band derives from nitrogen states *per se*, with the majority weight corresponding to states associated with the shifted carbon atom.

The ionization potential of the donor level of N_s has been estimated to be at E_c-2.0 eV and E_c-1.69 eV (EMM and FPMM resuts) and the acceptor level at E_c-1.1 eV (FPMM), results which are in good agreement with previous calculations and experimental evidences.[51,88,93] In particular, computed ionization potentials match well with the thresholds at 2.3 eV and 4.5 eV in photoconductivity. The former, which has been ascribed to the excitation of electrons, can be compared with the band observed in absorption at 2.2 eV; while the latter, which has been ascribed to the excitation of holes, fits with the broad absorption at 4.6 eV attributed to the transition of electrons from the valence band to the acceptor level of N_s.[93]

The C centre formation energy is estimated to be ∼3.6 eV, and as expected, is considerably lower than defects involving N aggregates.[57,58]

The IR spectrum in the region (900-1400) cm^{-1} is characterised by several peaks grouped round a strong central peak at 1125 cm^{-1} and by a few less intense peaks between 1320 cm^{-1} and 1340 cm^{-1}, which lie above the Raman frequency. These are in satisfactory agreement with the reported experimental spectrum of type *Ib* synthetic diamond.[27,32,33,36–38] Conversely, there are no significant features in the Raman spectrum other than the strong 1317 cm^{-1} absorption of the perfect crystal. This is within 1.1% of the measured value[31] of 1332 cm^{-1}, which verifies the accuracy of the present frequency simulations.

The calculated hyperfine constants related to the coupling of the unpaired electron spin to the N and C nuclei, for which the Fermi contact terms vary from over 200

MHz to less than 3 MHz, are generally in good agreement with the largest experimental values, both in terms of absolute magnitudes and site assignments. The sole exception is the $^{13}C_4$ constant, which is ∼11% greater than the reported values and is assigned to different site. The agreement is less good for the smallest two Fermi contact terms, for which the experimental assignments have been reported[41,42] to be less certain. The dependence of the hyperfine coupling tensor terms on computational parameters has been carefully addressed. From this it emerged that there is a substantial variation in the values of the hyperfine constants derived from different basis sets, with the 6-31G-J* set the preferred choice, but much less variation with functional, with PBE and LDA being the least effective. There is no significant difference between the S_{216} and S_{512} values, suggesting that the values of these constants are independent of defect concentrations.

* Electronic address: anna.ferrari@unito.it

[1] J.P. Bade, S.R. Sahaida, B.R. Stoner, J.A. Windheim, J.T. Glass, K. Miyata, K. Nishimura, and K. Kobashi. Fabrication of Diamond Thin-Film Thermistors for High Temperature Applications. *Diamond Relat. Mater.*, 2:816–819, 1993.

[2] D. Bergonzo, P and. Tromson and C. Mer. CVD Diamond-Based Semi-Transparent Beam-Position Monitors for Synchrotron Beamlines: Preliminary Studies and Device Developments at CEA/Saclay. *J. Sync. Rad.*, 13:151–158, 2006.

[3] G. B. B. M. Sutherland, D. E. Blackwell, and W. G. Simeral. The Problem of the Two Types of Diamond. *Nature*, 174:901–904, 1954.

[4] G. Davies. The A Nitrogen Aggregate in Diamond – its Symmetry and Possible Structure. *J. Phys. C*, 9:L537–L542, 10 1976.

[5] S. J. Breuer and P.R. Briddon. *Ab Initio* Investigation of the Native Defects in Diamond and Self-Diffusion. *Phys. Rev. B*, 51(11):6984–6994, 1995.

[6] A. Mainwood. Modelling of Interstitial-Related Defects in Diamond. *Diamond Relat. Mater.*, 8(8):1560–1564, 1999.

[7] R. Kalish, A. Reznik, S. Prawer, D. Saada, and J. Adler. Ion-Implantation-Induced Defects in Diamond and Their Annealing: Experiment and Simulation. *Phys. Status Solidi A*, 174(1):83–99, 1999.

[8] G. Davies, B. Campbell, A. Mainwood, M. Newton, M. Watkins, H. Kanda, and T.R. Anthony. Interstitials, Vacancies and Impurities in Diamond. *Phys. Status Solidi A*, 186(2):187–198, 2001.

[9] J. P. Goss, B. J. Coomer, R. Jones, C. J. Fall, P. R. Briddon, and S. Öberg. Extended Defects in Diamond: The Interstitial Platelet. *Phys. Rev. B*, 67:165208, Apr 2003.

[10] J. P. Goss, R. Jones, T. D. Shaw, M. J. Rayson, and P. R. Briddon. First Principles Study of the Self-Interstitial Defect in Diamond. *Phys. Status Solidi A*, 186(2):215–220, 2001.

[11] Gordon Davies, Hannah Smith, and H. Kanda. Self-Interstitial in Diamond. *Phys. Rev. B*, 62:1528–1531, 2000.

[12] R. Kalish, A. Reznik, K. W. Nugent, and S. Prawer. The Nature of Damage in Ion-Implanted and Annealed Diamond. *Nucl. Instrum. Meth. Phys. Res. B*, 148(1):626–633, 1999.

[13] D. J. Twitchen, D. C. Hunt, M. E. Newton, J. M. Baker, T. R. Anthony, and W. F. Banholzer. Electron Paramagnetic Resonance (EPR) and Optical Absorption Studies of Defects Created in Diamond by Electron Irradiation Damage at 100 and 350K. *Physica B: Cond. Matter*, 273:628–631, 1999.

[14] P. F. Lai, S. Prawer, and C. Noble. Electron Spin Resonance Investigation of Ion-Irradiated Diamond. *Diam. Relat. Mater.*, 11(7):1391–1396, 2002.

[15] A. Moroño, S. M. González de Vicente, and E. R. Hodgson. Radiation Effects on the Optical and Electrical Properties of CVD Diamond. *Fusion Eng. Des.*, 82(15):2563–2566, 2007.

[16] H. Amekura and N. Kishimoto. Effects of High-Fluence Ion Implantation on Colorless Diamond Self-Standing Films. *J. Appl. Phys.*, 104(6):63509, 2008.

[17] S. Prawer, I. Rosenblum, J. O. Orwa, and J. Adler. Identification of the Point Defects in Diamond as Measured by Raman Spectroscopy: Comparison between Experiment and Computation. *Chem. Phys. Lett.*, 390:458–461, 2004.

[18] D. Hyde-Volpe, B. Slepetz, and M. Kertesz. The [V−C=C−V] Divacancy and the Interstitial Defect in Diamond: Vibrational Properties. *J. Phys. Chem.*, 114(21):9563–9567, 2010.

[19] D. N. Jamieson, S. Prawer, K. W. Nugent, and S. P. Dooley. Cross-Sectional Raman Microscopy of MeV Implanted Diamond. *Phys. Rev. B*, 106:641–645, 1995.

[20] J. D. Hunn, S. P. Withrow, C. W. White, and D. M. Hembree Jr. Raman Scattering From MeV-Implanted Diamond. *Phys. Rev. B*, 52:8106–8111, 1995.

[21] S. Prawer, K. W. Nugent, and D. N. Jamieson. The Raman Spectrum of Amorphous Diamond. *Diam. Relat. Mater.*, 7:106–110, 1998.

[22] J. O. Orwa, K. W. Nugent, D. N. Jamieson, and S. Prawer. Raman Investigation of Damage Caused by Deep Ion Implantation in Diamond. *Phys. Rev. B*, 62(9):5461–5472, 2000.

[23] R. Brunetto, G. A. Baratta, and G. Strazzulla. Raman Spectroscopy of Ion Irradiated Diamond. *J. Appl. Phys.*, 96:380–386, 2004.

[24] P. Olivero, S. Rubanov, P. Reichart, B. C. Gibson, S. T. Huntington, J. R. Rabeau, A. D. Greentree, J. Salzman, D. Moore, D. N. Jamieson, and S. Prawer. Characterization of Three-Dimensional Microstructures in Single-Crystal Diamond. *Diamond Relat. Mater.*, 15:1614–1621, 2006.

[25] A. A. Bergman, A. M. Zaitsev, M. Huang, and A.A. Gorokhovsky. Photoluminescence and Raman Studies of Xe Ion-Implanted Diamonds: Dependence on Implantation Dose. *J. Lumin.*, 129:1524–1526, 2009.

[26] J.J. Charette. Absorption Spectra of Type I and Type II Synthetic Diamonds,. *J. Chem. Phys.*, 37:3014–3015, 1962.

[27] H.B. Dyer, F.A. Raal, L.Du. Preez, and J.H.N. Loubser. Optical Absorption Features Associated with Paramagnetic Nitrogen in Diamond. *Phil. Mag.*, 11:763–774,

1965.

[28] T. Evans, Z. Qi, and J. Maguire. The Stages of Nitrogen Aggregation in Diamond. *Journal of Physics C: Solid State Physics*, 14:L379, 1981.

[29] A. A. Zedgenizova, TD. A. anad A. A. Kalinina, V. V. Kalininaa, and Yu. N. Palyanova. The Transformation Features of Impurity Defects in Natural Diamonds of Various Habits under High PT Conditions. *Doklady Earth Sciences*, 466:32–37., 2016.

[30] S. C. Lawson, D. Fisher, D. C. Hunt, and M. E. Newton. On the Existence of Positively Charged Single-Substitutional Nitrogen in Diamond. *J. Phys. Condens. Matter*, 10(27):6171, 1998.

[31] A. M. Zaitsev. *Optical Properties of Diamond - A Data Handbook*. Springer-Verlag, 2001.

[32] A.T. Collins and G.S. Woods. An Anomaly in the Infrared Absorption Spectrum of Synthetic Diamond. *Philos. Mag. B*, 46:77–83, 1982.

[33] A.T. Collins, M. Stanley, and G.S. Woods. Nitrogen Isotope Effects in Synthetic Diamonds. *J. Phys. D*, 20:969–974, 1987.

[34] C. D. Clark and S. T. Davey. One Phonon Infrared Absorption in Diamond. *Phys. C Solid State*, 17:1127–1140, 1984.

[35] G. S. Woods. Platelets and the Infrared Absorption of Type Ia Diamonds. In *Proceedings of the Royal Society of London A: Mathematical, Physical and Engineering Sciences*, volume 407, pages 219–238. The Royal Society, 1986.

[36] Thomas Hainschwang, Emmanuel Fritsch, Franck Notari, and Benjamin Rondeau. A New Defect Center in Type Ib Diamond Inducing One Phonon Infrared Absorption: the Y Center. *Diamond and Related Materials*, 21:120–126, 2012.

[37] Thomas Hainschwang, Emmanuel Fritsch, L Massi, Benjamin Rondeau, and Franck Notari. The C Center Isolated Nitrogen-Related Infrared Absorption at 2688 cm^{-1}: Perfect Harmony in Diamond. *Journal of Applied Spectroscopy*, 79:737–743, 2012.

[38] Thomas Hainschwang, Emmanuel Fritsch, Franck Notari, Benjamin Rondeau, and Andrey Katrusha. The Origin of Color in Natural C Center Bearing Diamonds. *Diamond and Related Materials*, 39:27–40, 2013.

[39] W. V. Smith, P. P. Sorokin, I. L. Gelles, and G.J. Lasher. Electron-Spin Resonance of Nitrogen Donors in Diamond. *Phys. Rev.*, 1546–1553:2703, 1959.

[40] J. H. N. Loubser and L. Du Preez. New Lines in the Electron Spin Resonance Spectrum of Substitutional Nitrogen Donors in Diamond. *Br. J. App. Phys.*, 16(4):457, 1965.

[41] A. Cox, M. E. Newton, and JM Baker. ^{13}C, ^{14}N and ^{15}N ENDOR Measurements on the Single Substitutional Nitrogen Centre (P1) in Diamond. *J. Phys. Condens. Matter*, 6:551–563, 1994.

[42] RC Barklie and J Guven. ^{13}C Hyperfine Structure and Relaxation Times of the P1 Centre in Diamond. *J. Phys. C: Solid State Phys.*, 14:3621–3631, 1981.

[43] H.J. Bower and M.C.R. Symons. Electron Spin Resonance Spectra Associated with Nitrogen in Diamonds. *Nature*, 210:1037–1038, 1966.

[44] R.M. Chrenko, H.M. Strong, and R.E. Tuft. Dispersed Paramagnetic Nitrogen Content of Large Laboratory Diamonds. *Phil. Mag.*, 23:313–318, 1971.

[45] G.S. Woods, J.A. Van Wyk, and A.T. Collins. The Nitrogen Content of Type Ib Synthetic Diamond. *Phil. Mag. B*, 62:589–595, 1991.

[46] R. J. Cook and D. H. Whiffen. . *Proc. R. Soc. Lond. A*, 295:99–106, 1966.

[47] P. R. Briddon and R. Jones. Theory of Impurities in Diamond. *Phys. B*, 185:179–189, 1993.

[48] A. Mainwood. Nitrogen and Nitrogen-Vacancy Complexes and Their Formation in Diamond. *Phys. Rev. B*, 49:2010–2103, 1994.

[49] E.B. Lombardi, A. Mainwood, K. Osuch, and E.C. Reynhardt. Computational Models of the Single Substitutional Nitrogen Atom in Diamond. *J. Phys. Cond. Matter.*, 15:31353149, 2003.

[50] CV Peaker, MK Atumi, JP Goss, PR Briddon, AB Horsfall, MJ Rayson, and R Jones. Assignment of 13C Hyperfine Interactions in the P1-Center in Diamond. *Diamond and Related Materials*, 70:118–123, 2016.

[51] R.G Farrer. On the Substitutional Nitrogen Donor in Diamond. *Solid State Commun.*, 7:685–688, 1969.

[52] J. Walker. Optical Absortpion and Luminescence in Diamond. *Rep. Prog. Phys.*, 42:1605–1659, 1979.

[53] J. Baima, A. Zelferino, P. Olivero, A. Erba, and R. Dovesi. Raman Spectroscopic Features of the Neutral Vacancy in Diamond from *Ab Initio* Quantum-Mechanical Calculations. *Phys. Chem. Chem. Phys.*, 18(3):1961–1968, 2016.

[54] A. Zelferino, S. Salustro, J. Baima, V. Lacivita, R. Orlando, and R. Dovesi. The Electronic States of the Neutral Vacancy in Diamond: a Quantum Mechanical Approach. *Theor. Chem. Acc.*, 135(3):1–11, 2016.

[55] S. Salustro, A. Erba, C. M. Zicovich-Wilson, Y. Noël, L. Maschio, and R. Dovesi. Infrared and Raman Spectroscopic Features of the Self-Interstitial Defect in Diamond from Exact-Exchange Hybrid DFT Calculations. *Phys. Chem. Chem. Phys.*, 120:21288–21295, 2016.

[56] S. Salustro, Y. Noël, C. M. Zicovich-Wilson, P. Olivero, and R. Dovesi. The V+I Defects in Diamond: an *Ab Initio* Investigation of the Electronic Structure, of the Raman and IR Spectra, and of their Possible Recombination . *J. Chem. Phys.*, 145(18):184701, 2016.

[57] S. Salustro, G. Sansone, C. M. Zicovich-Wilson, Y. Noël, L. Maschio, and R. Dovesi. The A-center Defect in Diamond. A Quantum Mechanical Characterization Through the Infrared Spectrum. *Phys. Chem. Chem. Phys.*, 19:14478–14485, 2017.

[58] S. Salustro, A. M. Ferrari, F. S. Gentile, J. K. Desmarais, M. Rérat, and R. Dovesi. Characterization of the B-center Defect in Diamond Through the Vibrational Spectrum. A Quantum Mechanical Approach. *J. Phys. Chem. A*, 122(2):594–600, 2018.

[59] S: Salustro, A. M. Ferrari, R. Orlando, and R. Dovesi. Comparison Between Cluster and Supercell Approaches: the Case of Defects in Diamond. *Theor. Chem. Acc.*, 4(136):1–13, 2017.

[60] F. Gentile, S. Salustro, M. Causá, A. Erba, P. Carbonniére, and R. Dovesi. The VN_3H Defect in Diamond. A Quantum Mechanical Investigation of the Structural, Electronic and Vibrational Properties. *Phys. Chem. Chem. Phys.*, 1(4):1–2, 2017.

[61] S. Salustro, F. S. Gentile, P. D'Arco, B. Civalleri, M. Rérat, and R. Dovesi. Hydrogen Atoms in the Diamond Vacancy Defect. A Quantum Mechanical Vibrational Analysis. *Carbon*, 129:349–356, 2018.

[62] G. Sansone, S. Salustro, Y. Noël, L. Maschio, W. C. Mackrodt, and R. Dovesi. Looking for sp^2 Carbon Atoms in Diamond: a Quantum Mechanical Study of Interacting Vacancies. *Theor. Chem. Acc.*, 137(2):29, 2018.

[63] P. Hohenberg and W. Kohn. Inhomogeneous Electron Gas. *Phys. Rev.*, 136(3B):B864, 1964.

[64] W. Kohn and L. J. Sham. Self-Consistent Equations Including Exchange and Correlation Effects. *Phys. Rev.*, 140(4A):A1133, 1965.

[65] A. D. Becke. Density-Functional Thermochemistry. III. The Role of Exact Exchange. *J. Chem. Phys.*, 98(7):5648–5652, 1993.

[66] C. Lee, W. Yang, and R. Parr. Development of the Colle-Salvetti Correlation-Energy Formula Into a Functional of the Electron Density. *Phys. Rev. B*, 37(2):785–789, 1988.

[67] R. Dovesi, A. Erba, R. Orlando, C. M. Zicovich-Wilson, B. Civalleri, L. Maschio, M. Rérat, S. Casassa, J. Baima, S. Salustro, and B. Kirtman. Quantum-Mechanical Condensed Matter Simulations with CRYSTAL. *Wires*, 2018.

[68] P. Dirac. A Theory of Electrons and Protons. *Proc. R. Soc. A*, 126(801):360–365, 1930.

[69] S. H. Vosko, L. Wilk, and M. Nusair. Accurate Spin-Dependent Electron Liquid Correlation Energies for Local Spin Density Calculations: a Critical Analysis. *Can. J. of Phys.*, 58(8):1200–1211, 1980.

[70] J. P. Perdew, K. Burke, and M. Ernzerhof. Generalized Gradient Approximation Made Simple. *Phys. Rev. Lett.*, 77(18):3865–3868, 1996.

[71] C. Adamo and V. Barone. Toward Chemical Accuracy in the Computation of NMR Shieldings: the PBE0 Model. *Chem. Phys. Lett.*, 298(1):113–119, 1998.

[72] A. V. Krukau, O. A. Vydrov, A. F. Izmaylov, and G. E. Scuseria. Influence of the Exchange Screening Parameter on the Performance of Screened Hybrid Functionals. *J. Chem. Phys.*, 125(22):224106–224106, 2006.

[73] J. S. Binkley, J. A. Pople, and W. J. Hehre. Self-Consistent Molecular Orbital Methods. 21. Small Split-Valence Basis Sets for First-Row Elements. *J. Am. Chem. Soc.*, 102(3):939–947, 1980.

[74] H. Kjr and S. P. A. Sauer. Pople Style Basis Sets for the Calculation of NMR Spin-Spin Coupling Constants: the 6-31G-J and 6-311G-J Basis Sets. *J. Chem. Theory Comput.*, 7:4070–4076, 2011.

[75] A. D. Becke. A Multicenter Numerical Integration Scheme for Polyatomic Molecules. *J. Chem. Phys.*, 88(4):2547–2553, 1988.

[76] H. J. Monkhorst and J. D. Pack. Special Points for Brillouin-Zone Integrations. *Phys. Rev. B*, 13(12):5188, 1976.

[77] F. Pascale, C. M. Zicovich-Wilson, F. Lòpez Gejo, B. Civalleri, R. Orlando, and R. Dovesi. The Calculation of the Vibrational Frequencies of the Crystalline Compounds and its Implementation in the CRYSTAL Code. *J. Comput. Chem.*, 25(6):888–897, 2004.

[78] C. M. Zicovich-Wilson, F. Pascale, C. Roetti, V. R. Saunders, R. Orlando, and R. Dovesi. Calculation of the Vibration Frequencies of α-Quartz: The Effect of Hamiltonian and Basis Set. *J. Comput. Chem.*, 25(15):1873–1881, 2004.

[79] A. Erba, M. Ferrabone, R. Orlando, and R. Dovesi. Accurate Dynamical Structure Factors from *Ab Initio* Lattice Dynamics: The case of Crystalline Silicon. *J. Comput. Chem.*, 34:346–354, 2013.

[80] C. Carteret, M. De La Pierre, M. Dossot, F. Pascale, A. Erba, and R. Dovesi. The Vibrational Spectrum of $CaCO_3$ Aragonite: a Combined Experimental and Quantum-Mechanical Investigation. *J. Chem. Phys.*, 138(1):014201, 2013.

[81] J. Baima, M. Ferrabone, R. Orlando, A. Erba, and R. Dovesi. Thermodynamics and Phonon Dispersion of Pyrope and Grossular Silicate Garnets from *Ab Initio* Simulations. *Phys. Chem. Minerals*, 43:137–149, 2016.

[82] G. M. Barrow. *Introduction to Molecular Spectroscopy.* McGraw-Hill, New York, 1962.

[83] B. A. Hess, L. J. Schaad, P. Carsky, and R. Zahradnik. *Ab Initio* Calculations of Vibrational Spectra and Their Use in the Identification of Unusual Molecules. *Chem. Rev.*, 86:709–730, 1986.

[84] L. Maschio, B. Kirtman, R. Orlando, and M. Rérat. *Ab Initio* Analytical Infrared Intensities for Periodic Systems Through a Coupled Perturbed Hartree-Fock/Kohn-Sham Method. *J. Chem. Phys.*, 137(20):204113, 2012.

[85] L. Maschio, B. Kirtman, M. Rérat, R. Orlando, and R. Dovesi. Comment on "*Ab Initio* Analytical Infrared Intensities for Periodic Systems Through a Coupled Perturbed Hartree-Fock/Kohn-Sham Method" [J. Chem. Phys. 137, 204113 (2012)]. *J. Chem. Phys.*, 139:167101, 2013.

[86] L. Maschio, B. Kirtman, M. Rérat, R. Orlando, and R. Dovesi. *Ab initio* Analytical Raman Intensities for Periodic Systems Through a Coupled Perturbed Hartree-Fock/Kohn-Sham Method in an Atomic Orbital Basis. I. Theory. *J. Chem. Phys.*, 139(16):164101, 2013.

[87] L. Maschio, B. Kirtman, M. Rérat, R. Orlando, and R. Dovesi. *Ab Initio* Analytical Raman Intensities for Periodic Systems Through a Coupled Perturbed Hartree-Fock/Kohn-Sham Method in an Atomic Orbital Basis. II. Validation and Comparison with Experiments. *J. Chem. Phys.*, 139:164102, 2013.

[88] J.P. Goss, P.R. Briddon, R. Jones, and S. Sque. Donor and Acceptor States in Diamond. *Diamond and Related Materials*, 13:684–690, 2004.

[89] E. Gheeraert, S. Koizumi, T. Teraji, and H. Kanda. Electronic Transitions of Electrons Bound to Phosphorus Donors in Diamond. *Solid State Commun.*, 113(10):577–580, 2000.

[90] P. Deák, J. Miró, A. Gali, L. Udvardi, and H. Overhof. The Spin State of the Neutral Silicon Vacancy in 3C–SiC. *Appl. Phys. Lett.*, 75(14):2103–2105, 1999.

[91] R. Ulbricht, S. T. van der Post, J. P. Goss, P. R. Briddon, R. Jones, R. U. A. Khan, and M. Bonn. Single Substitutional Nitrogen Defects Revealed as Electron Acceptor States in Diamond Using Ultrafast Spectroscopy. *Phys. Rev. B*, 84:165202–1–165202–9, 2011.

[92] J. Rosa, M. Vanecek, M. Nesladek, and L.M. Stals. Single Substitutional Nitrogen Defects Revealed as Electron Acceptor States in Diamond Using Ultrafast Spectroscopy. *Diamond and Related Materials*, 8:721–724, 1999.

[93] K. Iakoubovskii and G. J. Adriaenssens. Optical Transitions at the Substitutional Nitrogen Centre in Diamond. *J. Phys.: Condens. Matter*, 12:L77–L81, 2000.

[94] R. Jones, J. P. Goss, and P. R. Briddon. Acceptor Level of Nitrogen in Diamond and the 270-nm Absorption Band. *Phys. Rev. B*, 80:033205–1–033205–4, 2009.

[95] C. D. Clark and S. T. Davey. Defect-Induced One-Phonon Absorption in Type Ia Diamonds. *Phys. C Solid State*, 17(15):L399, 1984.

[96] G. Davies. Decomposing the IR Absorption Spectra of Diamonds. *Nature*, 290(5801):40–41, 1981.

[97] T. Hainschwang, E. Fritsch, L. Massi, B. Rondeau, and F. Notari. The C Center Isolated Nitrogen-Related Infrared Absorption at 2688 cm^{-1}: Perfect Harmony in Diamond. *J. Appl. Spectrosc.*, 79(5):737–743, 2012.

[98] S. C. Lawson and H. Kanda. An Annealing Study of Nickel Point Defects in Highpressure Synthetic Diamond. *J. Appl. Phys.*, 73:3967–3973, 1993.
[99] A. T. Collins, P. J. Woad, G. S. Woods, and H. Kanda. Localised Vibrational Modes in Diamonds Grown from Mixed Carbon Isotopes. *Diamond and Related Materials*, 73:3967–3973, 1993.